

國立台灣大學理學院物理學系

碩士論文

Department of Physics

College of Science


National Taiwan University

Master Thesis

銫原子在中程紅外強場雷射中

產生低閾值與近閾值高次諧波機制之探究

Exploration of
the Mechanisms for Below- and Near-Threshold
High-Order Harmonic Generation of
Cesium Atoms in Intense Mid-Infrared Laser Fields



陳怡蓁

Yi-Jen Chen

指導教授：朱時宜博士

Advisor: Shih-I Chu, Ph.D.

中華民國 100 年 6 月

June, 2011

中文摘要

在這篇論文中，我們從非微擾的量子力學觀點，研究鉈原子在中程紅外強場雷射中產生高次諧波 (high-order harmonic generation, HHG) 的現象。我們建立了一個和角動量量子數有關的模型勢能，精準地描述了鉈原子的電子結構。我們以時變廣義擬譜方法 (time-dependent generalized pseudospectral method, TDGPS) 有效率且準確地求解了三維的時變薛丁格方程式。

除了預期的奇數高次諧波外，由於鉈原子 6s 與 np 能階間的強耦合，我們得到的高次諧波頻譜顯示了一些額外的結構。經由傅立業 (Fourier) 及小波 (wavelet) 分析，我們更進一步探索了高次諧波的時間與光譜特性。藉此我們可以瞭解在不同能量範圍之高次諧波產生的主要機制，特別是低閾值與近閾值 (below- and near-threshold) 高次諧波的產生。

Abstract

In this thesis, we present a non-perturbative quantum study of high-order harmonic generation (HHG) of Cesium atoms in intense mid-infrared laser pulses. An accurate angular-momentum--dependent model potential is constructed for the high-precision description of the Cs atom electronic structure. The three-dimensional time-dependent Schrödinger equation is solved accurately and efficiently by means of the time-dependent generalized pseudospectral (TDGPS) method.

Besides the expected odd harmonics, the calculated HHG spectra show additional structures due to the strong $6s - np$ couplings. The spectral and temporal characteristics of the HHG are further explored through Fourier and the wavelet transformation. As a result, we can investigate the prevailing mechanisms in different energy regimes, especially those contributing to the generation of below- and near-threshold harmonics.

謝辭

生命是人在世上最珍貴的禮物，謝謝曾經參與我念碩士的這段生活時光的所有人。僅將此論文獻給：指導教授朱時宜—悉心的指導、溫柔的鼓勵、還有滿滿對學術及生命的熱忱，年輕人看了莫不自覺慚愧而想更加努力。口試委員孔慶昌、鄭王曜、及管希聖博士在口試時的提問讓氣氛活躍，建議對我幫助良多，點頭與微笑使我鎮定與有自信。訪問學者 Dr. D. A. Telnov 與 Dr. X. M. Tong 在遙遠的俄國與日本用 email 分享雄厚的數值經驗及協助我解決物理問題，以及 Dr. C. Laughlin 建造了鉅原子的模型勢。研究室成員 Dr. H. T. Heslar 以 80 歲純熟的數值與電腦技巧使我成長和 8 歲的牙牙學語帶來歡樂，陳信達讓我發現生活與工作平衡的重要性，游至安對各類數理問題的熱情與實力還有對人文的關懷，以及鄭富元、mark、王小明、二小姐、劉怡麟和我討論研究和生活上帶來的樂趣。我的家人對這個任性的女兒的諒解，當她閉關用功、脾氣暴躁時，溫柔在背後默默給予支持；外婆和奶奶在今年初離開我們，總是以我為傲，我卻因為學業而疏於探望... 最親愛的男友冠文在這段時間無微不至地陪伴、聆聽我，和我分享一切悲傷沮喪或者快樂，給我力量與勇氣；還有他介紹我認識的網球選手 Rafeal Nadal，在最後與口試、論文、GRE 奮鬥的時候，他在球場上的表顯提醒我：良好的心理素質、冷靜與持之以恆才是致勝的關鍵。

Contents

中文摘要	i
Abstract	ii
謝辭	iii
Contents	iv
List of Figures	vi
List of Tables	viii
1 Introduction	1
1.1 Strong field physics	1
1.2 Fundamentals of HHG	2
1.3 HHG mechanisms in two extremes	3
1.4 Below- and near-threshold harmonics	8
1.5 Cesium in the mid-infrared laser pulses	8
2 Numerical Methods	10
2.1 Difficulties in solving the HHG problem	10
2.2 The Time-dependent Schrödinger equation	11



2.3	Angular-momentum--dependent model potential for Cesium	12
2.4	Time-dependent generalized pseudospectral method	14
2.5	Summary	17
3	Results and Discussions	18
3.1	Laser characteristics and quantum dynamics	18
3.2	Fourier analysis: spectral properties of HHG	25
3.3	Fourier analysis: temporal properties of the HHG	31
3.4	Wavelet analysis: spectral and temporal properties of the HHG	34
3.5	Summary	39
4	Conclusions and Future Perspectives	41
	Bibliography	43



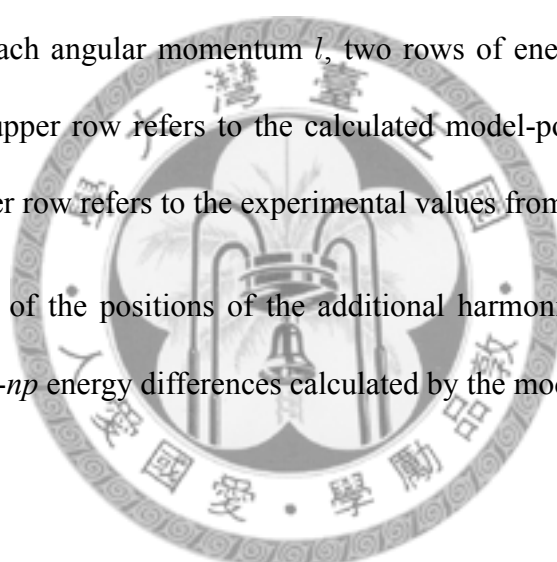
List of Figures

1.1	Generic harmonic spectrum. This is an experimental result generated using Ar and a 1064nm Nd:YAG laser at an intensity approximately $3 \times 10^{13} W/cm^2$. Reproduced from [1].	3
1.2	Illustration of the multiphoton process.	4
1.3	Illustration of how the semi-classical three-step model describes the HHG process. Reproduced from [2]	5
1.4	Electron return time versus return energy calculated by the semi-classical three-step model. Reproduced from [3].	7
2.1	Typical grid distribution for atomic HHG calculations using the TDGPS method.	16
3.1	Typical laser pulse used in the present calculation. $\lambda = 3600nm, \tau_{FWHM} = 110fs$, and $I = 2.1TW/cm^2$	20
3.2	Time-dependent ion population (orange solid line). The absolute value of the laser pulse is also shown (green dotted line) for comparison.	21
3.3	Time-dependent induced dipole moment in length form (panal (a)) and acceleration form (panal (b)).	24
3.4	Comparison dipole accelerations in two different intensities.	25

3.5	Calculated harmonic spectrum $P(\omega)$ from dipole acceleration.	28
3.6	Comparison of the below- and near-threshold harmonics. Panel (a) experimental result, reproduced from [4]; panel (b) theoretical result.	29
3.7	HHG power spectrum in the low intensity $I = 1.0TW/cm^2$ case. Panel(a) rescaled below- and near-threshold harmonics; panel (b) the whole HHG spectrum.	30
3.8	Calculate group delay with laser intensity $I = 2.1TW/cm^2$	33
3.9	Group delay of the below- and near-threshold harmonics. Panel (a) shows the experimental results (blue solid line), reproduced from [4]; panel (b) is our calculated emission times (pink dots).	34
3.10	Time-frequency spectrum of atomic Cs. The color represent the modulus of $d_\omega(t)$ in logarithmic scale.	36
3.11	Typical time profiles of HHG for (a) the lowest few harmonics, (b) below- and near-threshold harmonics, (c) plateau harmonics, and (d) cut-off harmonics.	37
3.12	Evolution of the time profiles of the below- and near-threshold harmonics.	39
3.13	Typical time profile for a peak due to the multiphoton resonance between two strongly coupled states, here the $6s$ and $6p$ states.	40

List of Tables

2.1	Model potential parameters for Cs (in a.u.).	13
2.2	Comparison of the calculated Cs energies to the experimental values (in a.u.). For each angular momentum l , two rows of energies $E(n, l)$ are listed: the upper row refers to the calculated model-potential energies, and the lower row refers to the experimental values from [5].	14
3.1	Comparison of the positions of the additional harmonic peaks and the field-free $6s$ - np energy differences calculated by the model potential. . . .	31



Chapter 1

Introduction

In this chapter, the rudimentary knowledge of high-harmonic generation and the motivations for this work are introduced.

1.1 Strong field physics

Our first grasp of the interaction between atoms, molecules, and photons initiates from Einstein's law for the photoelectric effect. This law, justified formally by the lowest-order perturbation theory and Fermi's golden rule, is strictly concerned with the absorption of a *single photon* during a transition. Nevertheless, moving in pace with the advance of the available laser intensities, the interaction has now entered the *non-perturbative* regime, where the strength of the of the laser field is comparable to that of the Coulomb binding force of the atomic core exerting on the active electron and *non-linear multiphoton* transition appears.

After the multiphoton absorption of several soft photons, the electron of the target X gets some chance to recombine into the ground state by emitting a hard photon with an

energy q times the incident photon $\hbar\omega_0$:

$$X + q(\hbar\omega_0) \longrightarrow X + (q\hbar\omega_0), \quad (1.1)$$

where q is an integer. When a relative intense laser is used as the light source, harmonics have been observed to very high order. For example, Colosimo et al. [6] have observed a highest 355th harmonic using Argon and a $2\mu\text{m}$ 50fs laser pulse. This phenomenon is named *high-order harmonic generation (HHG)*, and is the primary physical process we concern in this thesis.

1.2 Fundamentals of HHG

A generic HHG spectrum is shown in Figure 1.1: there is an initial *sharp decline* in conversion efficiency, then a *plateau* where the harmonic intensity varies weakly with order, and eventually a *cut-off* beyond which no harmonic emission is seen. Typically only odd harmonics are observed if the Hamiltonian of the system has inversion symmetry. In addition to pure theoretical interests, HHG has several applications. For instance, while using rare-gas atoms and short laser pulses in the near-visible or UV regime, the coherently generated harmonic can extend to the XUV ($\lambda = 10 - 120\text{nm}$) or even the soft X ray ($0.1 - 10\text{nm}$) water window region ($2.33 - 4.33\text{nm}$) [7, 8], a so called table-top synchrotron. Moreover, due to the fact that the HHG spectrum has a large bandwidth, it provides a practical means of synthesizing unprecedentedly short pulses on the order of attoseconds (10^{-18}s), which is the intrinsic time scale of the electron motion in atoms or molecules. Up to now, an 80as isolated pulse has been generated by Krausz et al. [9], and

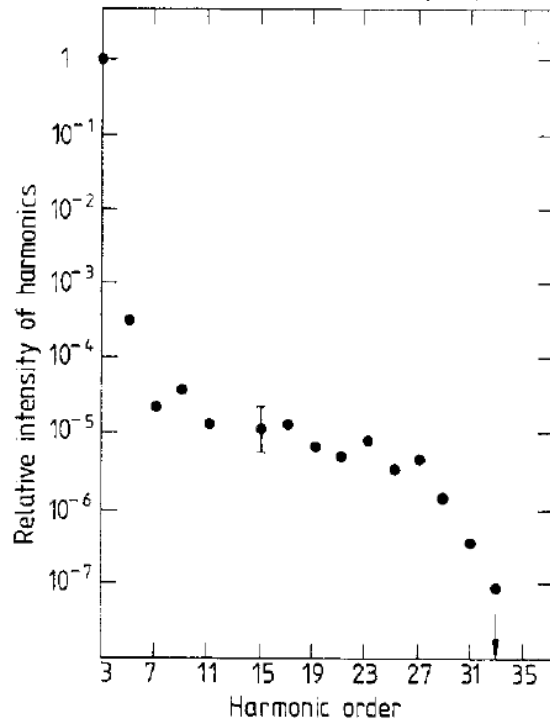


Figure 1.1: Generic harmonic spectrum. This is an experimental result generated using Ar and a 1064nm Nd:YAG laser at an intensity approximately $3 \times 10^{13} W/cm^2$. Reproduced from [1].

a 130as pulse train has been produced by L'Huillier et al [10].

1.3 HHG mechanisms in two extremes

The abrupt change of the trend of the harmonic conversion efficiency from the rapid decline to the plateau in Figure 1.1 implies a switch of different HHG mechanisms in the two energy regimes. These two regimes are separated roughly by the field-free ionization threshold I_p .

The formation of harmonics with energies *well below* I_p is due to *bound-bound excitation* process and can be explained by *mutiphoton mechanism*: an electron absorbs several

photon simultaneously, jumps to a (virtual) bound state, and then recombines into the ground state by emitting a high-energy photon, as schematically shown in Figure 1.2. In fact, owing to AC Stark effect, the ionization potential is constantly changing with time. Hence, strictly speaking, this familiar picture may be appropriate to describe only the lowest few harmonics, which involve transitions between low-lying states not that sensitive to AC Stark shift.

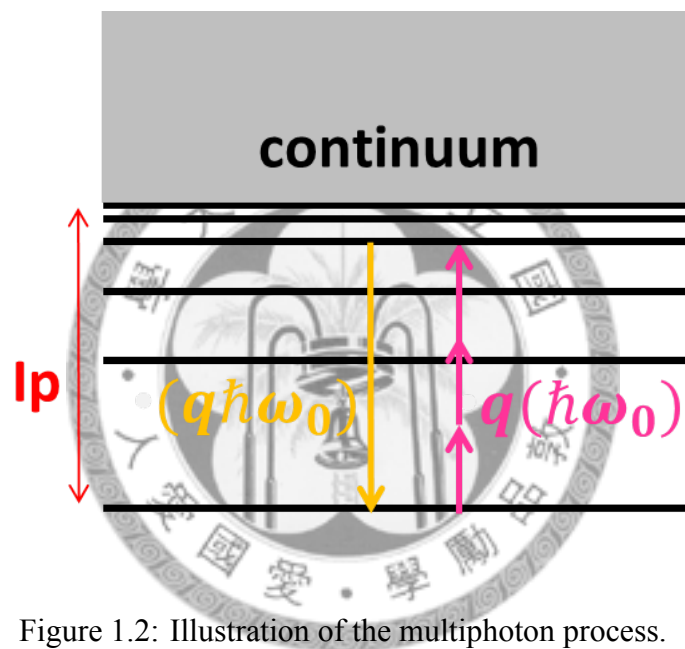


Figure 1.2: Illustration of the multiphoton process.

On the other hand, the generation of harmonics with energies *well above* I_p is related to *bound-continuum ionization* process. Under certain circumstances (we will discuss them later), the ionization process is realized in terms of Keldysh tunnelling mechanism [11]. In 1993, P. B. Corkum proposed a semi-classical three step model [12, 13] based on this assumption. This model is capable of predicting some essential features of HHG in an intuitive way. It depicts the HHG process as composed of the following three steps:

- First step (see Figure 1.3 a): purely quantum. The electron is launched by the *Keldysh tunnelling ionization*. The time-dependent laser field varies continuously

with time and keeps modifying the atomic Coulomb potential. When the field strength reaches the maximum, the Coulomb potential is severely suppressed, and the electron has the highest probability to tunnel through the modified potential barrier and gets ionized.

- Second step (see Figure 1.3 b): purely classical. The motion of the electron after liberation is then described *classically* by Newton's second law. The electron moves freely in the laser field and the effect of the nuclear Coulomb attraction is ignored.
- Third step (see Figure 1.3 c and d): purely quantum. When the laser field reverses its direction, the ionized electron might be pulled back and *rescattered* by the Coulomb potential. If the electron recollides with the parent ionic core, it gets some chance to recombine into the ground state and emits a high-energy photon.

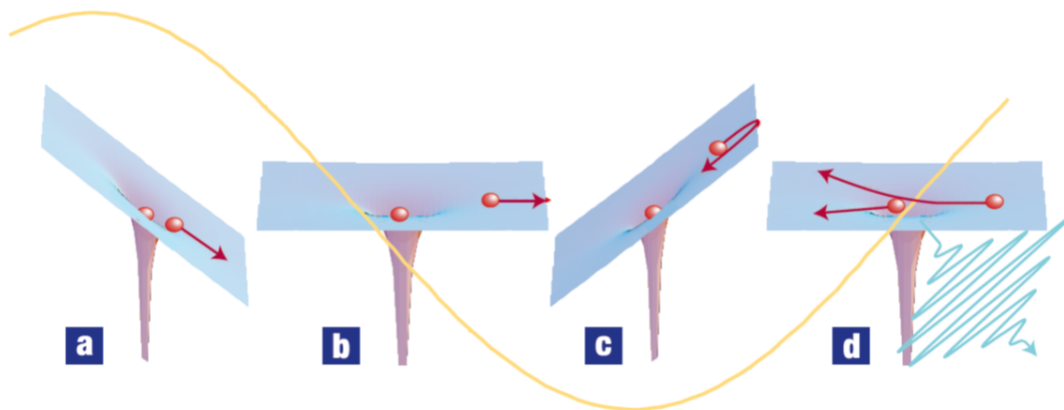


Figure 1.3: Illustration of how the semi-classical three-step model describes the HHG process. Reproduced from [2]

Conventionally, the concept of tunnelling is applicable only when the potential is time-independent. Nevertheless, as the change of the laser field is slow enough, the validity of

the tunnelling ansatz is assured under the adiabatic approximation, i.e.

$$\text{Keldysh adiabatic parameter } \gamma = \frac{\text{tunnelling time}}{\text{laser period}} = \sqrt{\frac{I_p}{2U_p}} \ll 1, \quad (1.2)$$

where $U_p = \frac{E^2}{4\omega^2}$ is the ponderomotive energy, that is, the average kinetic energy acquired by a free electron in a laser field of amplitude E and frequency ω . From the above relation, we can see that this approximation becomes better when the laser intensity is relatively high or laser wavelength is long. The harmonic energy predicted by the semi-classical model is:

$$\text{Harmonic energy} = \text{kinetic energy of the rescattering electron} + I_p \geq I_p. \quad (1.3)$$

Hence, this model can only explain the harmonic with energy greater than the ionization threshold. Actually, it can only account for the harmonic with energy much greater than I_p , for which the ignorance of Coulomb attraction after ionization has less influence.

The tunnelling mechanism is intrinsically different from the multiphoton mechanism. For the harmonic generated by the tunnelling mechanism, the electron gains energy *far away* from the core through the classical motion; this process is highly sensitive to the detailed laser pulse shape (both the pulse *envelope* and *carrier*), since it happens whenever the field strength reaches maximum. On the contrary, for the harmonic formed by the multiphoton mechanism, the electron gains energy *near* the ionic core; this procedure is only sensitive to the pulse shape in an averaged way, i.e. the pulse *envelope*, as predicted by the lost-order perturbation theory (LOPT) [14]. There is another way to distinguish the harmonic radiation between the two mechanisms by the relative emission times of successive

harmonics, dubbed the harmonic *chirp*. For the harmonics due to multiphoton mechanism, LOPT predicts the successive harmonics are emitted simultaneously (*zero chirp*). As for the harmonics resulting from the tunnelling mechanism, the situation becomes a little more complicated. Based on the semi-classical three-step model, if we select the main contributions, i.e. the electron tunnels out near some field strength maximum and returns to the ionic core within one laser period, and plot the return time versus return kinetic energy, we can get something similar to Figure 1.4. From this figure, we are able to

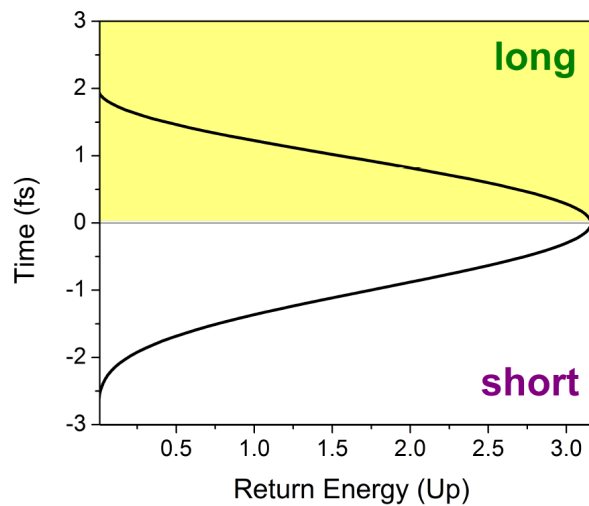


Figure 1.4: Electron return time versus return energy calculated by the semi-classical three-step model. Reproduced from [3].

see that there are two return times corresponding to each return energy. The one coming back earlier is named *short trajectory*, while the other returning later is called *long trajectory*. Compared with the long trajectory, short trajectory gets ionized later and recollides with the core earlier, thus travels within a shorter time and distance. We can get another important message from the figure: the emission times of the successive harmonics show different trends for the two kinds of trajectories. The high-frequency harmonic emits *after* the low-frequency one for short trajectories (positive slope, *positive chirp*), while the high-frequency component emits *before* the low-frequency one for long trajectories (negative

slope, *negative* chirp). Because the probabilities of generating short or long trajectories are generally not equal, the harmonic radiation originates from the tunnelling mechanism leads to a total *non-zero chirp*. In conclusion, we can explore the mechanism of harmonic generation by examining its chirp rate.

1.4 Below- and near-threshold harmonics

In the last section, we have discussed the HHG mechanism in two energy extremes. However, the mechanism accounting for generating the harmonics near or below the ionization threshold is relatively unexplored and a area of forefront research. Conventionally, only the multiphoton mechanism is considered to be responsible for the HHG in this regime. However, recent experimental studies [4, 15, 16] have found the tunnelling mechanism, especially the long trajectories, can also make its contribution here. In this thesis, we would like to scrutinize the HHG in this energy regime from a theoretical, full-quantum, and accurate point of view.

1.5 Cesium in the mid-infrared laser pulses

In [4], E. P. Power et al. performed the experiments by using an intense mid-infrared pulse shining on cesium gases. This work has fully exploited the Keldysh scaling property. Since the same ionization dynamics is guaranteed as long as the Keldysh parameter $\gamma = \sqrt{\frac{2I_p\omega^2}{E^2}}$ is fixed, we are provided the freedom to tune and select the appropriate physical parameters. For example, argon ($I_p = 15.76eV$) driven with a $130TW/cm^2$, $0.8\mu m$ pulse and cesium ($I_p = 3.89eV$) driven with a $1.6TW/cm^2$, $3.6\mu m$ pulse both produce

$\gamma = 1$. We say that a $3.6\mu\text{m}/\text{Cs}$ system is the Keldysh-scaled equivalent of the $0.8\mu\text{m}/\text{Ar}$ system. The advantage of using the mid-infrared light source is that some of the harmonics have wavelength in the visible region, so the conventional optical techniques, for example cross-correlation technique in [4], can be used to measure the *spectral* as well as the *temporal* properties of the HHG.

Since Cs belongs to alkali metals, another interesting property of the $3.6\mu\text{m}/\text{Cs}$ system is that the ground state ($6s$) and the first excited state ($6p$) has relatively strong coupling [17]. Some experimental and theoretical studies of potassium and rubidium [18, 19, 20, 21] have found this coupling leads to enhancement of the harmonic conversion efficiency. There have already been some experiments using cesium [22, 23], but no similar enhancement has been reported.

In the end of this chapter, we list the motivations for this current work as follows:

- We would like to perform the first 3D, quantum, and accurate calculation of HHG of Cs.
- Based on the calculation, we would like to explore the mechanisms of below- and near-threshold harmonic generation from a theoretical, single-atom point of view, and made comparison with the experimental result in [4].
- We would like to investigate the influence of the strong $6s - sp$ coupling of the Cs atom on HHG.

Chapter 2

Numerical Methods

In this chapter, we introduce different approaches in solving the strong-field problems, our theoretical formulation, and the numerical methods involved in this thesis.

2.1 Difficulties in solving the HHG problem

When the strength of the laser field is comparable to that of the Coulomb field binding the active electron, the HHG process is highly non-perturbative and no longer has any analytical solutions; we can only tackle the problem either by model or numerical calculations. The most famous semi-classical three-step model [12] has already been introduced in chapter 1. Similar quantum mechanical formalism, which also ignores the influence of the Coulomb potential when the electron gets tunnelingly ionized, is the strong-field approximation (SFA) [24]. The above two models can be linked together by the Feynman's path-integral approach [25], which considers the SFA as the net result of interference between a few trajectories.

These models definitely give us a lot of physical insights into the mechanism of the

HHG process. However, as we have seen before, the HHG process is highly non-linear and the signals cover a broad range of orders, hence the assumptions and approximations made by these models might sometimes be over simplistic and lead to the unpredictable results which differ from the experimental ones as large as several orders of magnitude [26]. Therefore, accurate numerical simulation plays an indispensable role in solving the strong-field problems. The most common numerical recipes are the time-independent non-Hermitian Floquet Hamiltonian methods [27] and direct numerical integration of the time-dependent Schrödinger equation [28, 29]. The former approach provides better numerical accuracy and computational efficiency, while the latter has more flexibility, regarding that it does not impose any constraint on the forms of the Hamiltonians and the shapes of the laser pulses. In this thesis, we adopt the direct numerical integration technique.

2.2 The Time-dependent Schrödinger equation

Here we consider the numerical solution to the time-dependent Schrödinger equation (TDSE) for a Cesium atom in a linearly polarized intense mid-infrared laser pulses treated classically (in atomic units):

$$i \frac{\partial}{\partial t} \Psi(\mathbf{r}, t) = H(t) \Psi(\mathbf{r}, t) = [H_0 + V_{ext}(t)] \Psi(\mathbf{r}, t). \quad (2.1)$$

Here H_0 is the time-independent unperturbed Cs-atom Hamiltonian, and $V_{ext}(t)$ is the time-dependent atom-laser coupling.

In the scheme of model potential methods, we describe a multi-electron atom as va-

lence electrons interacting with an effective closed shell. In the case of Cs, one kind of the alkali metals, solving TDSE then reduces to an one-electron three-dimensional problem: $\Psi(\mathbf{r}, t)$ is the wavefunction for the 6s valence electron, which moves under the influence of the Cs^+ core with electronic configuration $1s^2 2s^2 2p^6 3s^2 3p^6 3d^{10} 4s^2 4p^6 4d^{10} 5s^2 5p^6$. Based on the above single-active-electron (SAE) approximation, H_0 has the following form:

$$H_0 = \left(-\frac{1}{2} \frac{\partial^2}{\partial r^2} + \frac{L^2}{2r^2} \right) + V_c, \quad (2.2)$$

where V_c is a model potential for the Coulomb interaction between the 6s electron and the Cs^+ core. We shall discuss the detail of V_c in the next section. The atom-field coupling $V_{ext}(t)$ under dipole approximation now becomes

$$V_{ext}(t) = V_{ext}(\mathbf{r}, t) = -\mathbf{F}(t) \cdot \mathbf{r} = -F(t)z, \quad (2.3)$$

where $\mathbf{F}(t)$ is the time-dependent laser force, assumed polarized along the z direction.

2.3 Angular-momentum--dependent model potential for Cesium

For the present study, we have constructed a *high-precision* angular-momentum--dependent model potential to describe accurately the Coulomb interaction V_c :

$$V_c = \sum_l |Y_l^0\rangle V_l(r) \langle Y_l^0|, \quad (2.4)$$

$$V_l(r) = -\frac{1}{r} - \frac{\alpha}{2r^4} W_6\left(\frac{r}{r_c}\right) - \left(\frac{N - S_l}{r} + A_{1,l} \right) e^{-B_{1,l}r} - \left(\frac{S_l}{r} + A_{2,l} \right) e^{-B_{2,l}r}, \quad (2.5)$$

where α is the Cs^+ core dipole polarizability, r_c the effective Cs^+ core radius, N the number of the core electrons, and W_n a core--cut-off function given by

$$W_n(x) = 1 - \left[1 + nx + \frac{(nx)^2}{2!} + \cdots + \frac{(nx)^n}{n!} \right] e^{-nx}. \quad (2.6)$$

Note that the indexes of some parameters and thus their values have l -dependency. Here we find it is sufficient to use a 2-component model potential, that is, we have two different sets of parameters for the description of the states with $l = 0$ and $l \geq 1$ respectively. The numerical values of the parameters are listed in Table 2.1. The bound state energies predicted by the model potential are compared with the experimental values [5] in Table 2.2. The oscillator strength of the $6s - 6p$ transition is calculated to be 0.403, compared to the 0.394 expected for Cs.

Table 2.1: Model potential parameters for Cs (in a.u.).

l	α	r_c	S	N	A_1	A_2	B_1	B_2
0	15.6	3.35	59.151687	54	32.329367	0	1.69	4.67
≥ 1	15.6	3.35	41.035779	54	0.32427851	30	1.20	5.00

Table 2.2: Comparison of the calculated Cs energies to the experimental values (in a.u.). For each angular momentum l , two rows of energies $E(n, l)$ are listed: the upper row refers to the calculated model-potential energies, and the lower row refers to the experimental values from [5].

		$E(n, l)$					
$l \setminus n$	6	7	8	9	10	11	12
0	-0.1430990	-0.0586446	-0.0323015	-0.0204845	-0.0141531	-0.0103645	-0.0079174
	-0.1430990	-0.0586446	-0.0323014	-0.0204845	-0.0141531	-0.0103645	-0.0079174
1	-0.0904543	-0.0434199	-0.0257368	-0.0170564	-0.0121389	-0.0090812	-0.0070498
	-0.0904839	-0.0433784	-0.0257093	-0.0170393	-0.0121279	-0.0090737	-0.0070446
2	-0.0767537	-0.0401010	-0.0243947	-0.0163741	-0.0117426	-0.0088300	-0.0068826
	-0.0767685	-0.0400591	-0.0243586	-0.0163493	-0.0117259	-0.0088183	-0.0068719
3	-0.0316125	-0.0202221	-0.0140293	-0.0102970	-0.0078767	-0.0062189	-0.0050341
	-0.0315953	-0.0202086	-0.0140200	-0.0102907	-0.0078723	-0.0062157	-0.0050317
4	-0.0200405	-0.0139152	-0.0102218	-0.0078248	-0.0061817	-0.0050066	-0.0041372
	-0.0200407	-0.0139152	-0.0102217	-0.0078248	-0.0061817	-0.0050066	-0.0041372

2.4 Time-dependent generalized pseudospectral method

We directly discretize and numerically integrate Eqn. 2.1 by the time-dependent generalized pseudospectral method (TDGPS) developed by Tong and Chu et al [28, 30, 31, 32]. Pseudospectral methods belong to one type of discretization schemes which minimize the error by requiring the equation to be exactly satisfied at each spatial grid. They possess the simplicity of the direct discretization methods such as the finite difference (FD) and the finite element (FE) methods, while simultaneously maintain high accuracy and fast convergency of the finite basis set variational methods. They have been widely applied to solving the problems in fluid dynamics for some time, yet what making them become a perfect tool in handling the problems in strong-field atomic and molecular physics are the *generalizations* made by our former group members.

The most notable and important ingredients of these generalizations are in two respects: the non-uniform and optimal spatial grid discretization as well as the accurate and efficient time propagation achieved by the split-operator technique in the energy representation. For atomic or molecular structure calculations involving the Coulomb or Coulomb-like potential, one typical problem associated with the commonly used equal-spacing grid methods is the Coulomb singularity in the origin and the long-range nature of the potential. Generally, one either uses a soft potential or truncates the semi-infinite radial domain $[0, \infty)$ into a finite one $[r_{min}, r_{max}]$. The first treatment modifies the potential near the origin, which might have unpredictably large impact on the results through the non-linear effects. The second one has to use sufficiently small r_{min} and very large r_{max} , thus leads to the need of tremendous number of grids and makes the cost of calculations prohibitive. We can solve this problem by a *non-uniform* discretization of grids: it allows denser grids near the origin, where the environment changes most dramatically and the most crucial physics related to HHG happens, and a sparser mesh for the outer regime, where the potential varies slowly and radiative recombination is less possible. Accordingly, we have the optimal and the most efficient way to distribute and fully exploit all the grid points, and can get highly accurate wavefunction and the converged results with modest number of grids, often orders of magnitude smaller than those used in conventional equal-spacing discretization methods [30]. A typical distribution of the collocation points for atomic HHG calculations is shown in Figure 2.1.

The second feature of the TDGPS method is the time propagation by means of a novel second-order split operator technique in the energy-coordinate representation:

$$\Psi(t + \Delta t) = e^{-iH_0 \frac{\Delta t}{2}} e^{-iV_{ext}(t + \frac{\Delta t}{2})\Delta t} e^{-iH_0 \frac{\Delta t}{2}} \Psi(t) + \mathcal{O}(\Delta t^3) \quad (2.7)$$

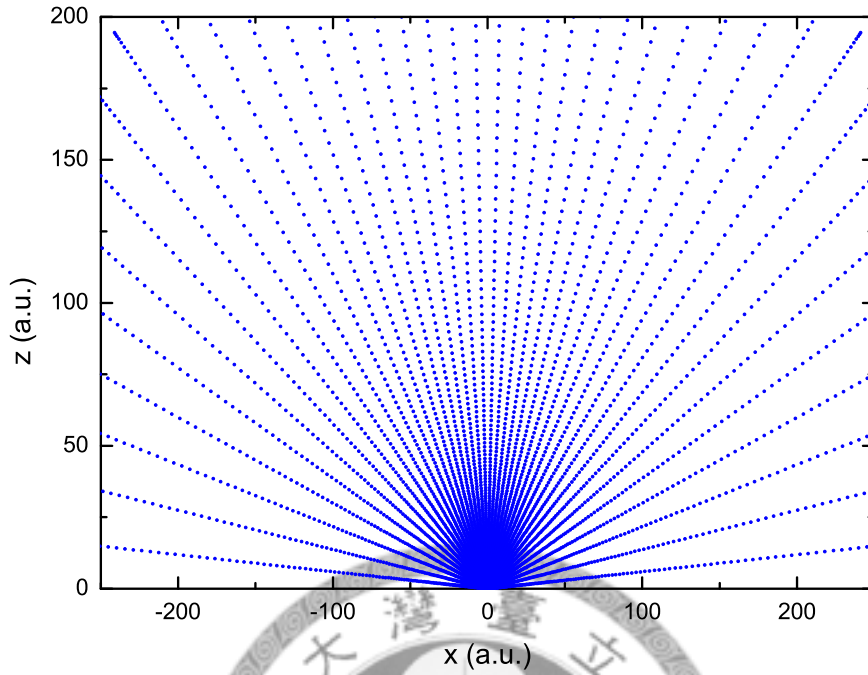


Figure 2.1: Typical grid distribution for atomic HHG calculations using the TDGPS method.

The conventional split-operator technique [33] splits the operator into kinetic and potential energy parts and performs the time propagation in momentum-coordinate representation. Both the conventional and the new split-operator method share the merits that the error in each time step is to the third order of Δt and the unitarity of the wavefunction is automatically preserved. However, the new split-operator method has the additional advantages that we can employ larger Δt by eliminating the undesirable and unstable high-energy components of the wavefunction, and that each partial wave wavefunction can actually be propagated independently and efficiently using the BLAS subroutines. Once the time-dependent wavefunction is known, we can calculate any physical quantities by computing the expectation value of the corresponding operator.

Until now, the efficiency and the accuracy of the TDGPS procedure have made it a powerful and successful tool in unravelling a variety of problems, such as the Hydrogen Rydberg-atom high-resolution spectroscopy [34], the creation and control of a single attosecond xuv pulse by synthesizing the H atom HHG in few-cycle intense laser pulses [35, 36], and spectral and temporal structures of HHG of Sodium [37]. It can also solve the problems of diatomic molecules in strong laser fields, take for example, the ab initio study of the orientation effects in multiphoton ionization and HHG of H_2^+ [38]. In addition to solving TDSE, it is capable of providing solution to the time-dependent density functional theory, see [39] for the HHG of H_2 and [40] for the HHG of both homonuclear and heteronuclear diatomic molecules.

2.5 Summary

In this chapter, we discuss the numerical details in solving the problem of HHG of Cs. First, we construct an accurate one-electron angular-momentum--dependent model potential for the high-precision description of the Cs atom. Then, the three-dimensional TDSE is solved nonperturbatively by means of the TDGPS method, which utilizes a non-uniform and optimal spatial grid discretization as well as a unconventional split-operator technique for the accurate and efficient propagation of the wavefunction in space and time.

Chapter 3

Results and Discussions

In this chapter, we present and discuss the results of HHG of Cs obtained by the numerical methods described in Chapter 2. We should discuss both the spectral and temporal characteristics of the HHG, and pay special attention to the behavior of the below- and near-threshold harmonics and compare our results with the experimental ones [4].

3.1 Laser characteristics and quantum dynamics

One of our motivations for the present work is to make comparison of our theoretical studies with the experiments carried out by E. P. Power et al. [4], where they surveyed the temporal and spectral properties of the below- and near-threshold harmonics of Cs gas in mid-infrared laser pulses using the sum frequency generation cross-correlation frequency resolved optical gating (SFG XFROG) technique. In their work, they have generated a laser pulse with central wavelength $\lambda = 3600 \text{ nm}$ and $\tau_{FWHM} \cong 110 \text{ fs}$. They estimated a maximum laser intensity $I = 2.66 \text{ TW/cm}^2$. Nevertheless, since the length of the Cs column in the experiments was approximately equal to the Rayleigh length of the focused fundamental beam, an exact value for the generating intensity for the harmonics can not

be given. In theoretical consideration, if we really use a $2.66TW/cm^2$ pulse to run the calculation, we find that the electron population is rapidly depleted before the laser intensity reaches its maxima. Thus, we have to use an intensity lower than $2.66TW/cm^2$. However, if the laser intensity is too weak, tunnelling mechanism is less applicable and the generation of long and short trajectories is irregular (we expect this by performing the classical calculations). In addition, in weak intensity, resonance prevails and will put extra and undesirable contribution on the temporal characteristics of HHG. Briefly, there is a compromise in choosing the laser intensity.

For our final data, we use a laser pulse with $\lambda = 3600nm$, $\tau_{FWHM} = 110fs$, $I = 2.1TW/cm^2$: $F_{max}f(t)\cos(\omega_0t)$, where F_{max} is the field amplitude, $f(t)$ a Gaussian envelope, and ω_0 the laser central frequency(see Figure 3.1). Under this condition, the Keldysh parameter $\gamma \cong 0.875 < 1$, so the tunnelling mechanism dominates. The data with $I = 1.0TW/cm^2$ are occasionally shown and compared, which has $\gamma \cong 1.27 > 1$ and is in the multiphoton regime. The primary numerical parameters for the TDGPS calculations are as follows: we use at least 400 radial grids ,90 partial waves, and an absorber placed in a large distance, typically over 200 a.u. Note that the strong-field calculations for Cs in intense mid-infrared laser pulses demand a much larger amount of partial waves in comparison with the cases of Hydrogen atoms or diatomic molecules. This means that the wavefunction tends to spread out extensively, and that the angular resolution plays an important role in this system. Therefore, theoretical treatments of this system based on some one-dimensional model potential, for example in [4], is not fairly proper. We run the time propagation for 40 optical cycles (O.C.), so that the laser field strength in the beginning and the end of the pulse is less than $10^{-5}F_{max}$.

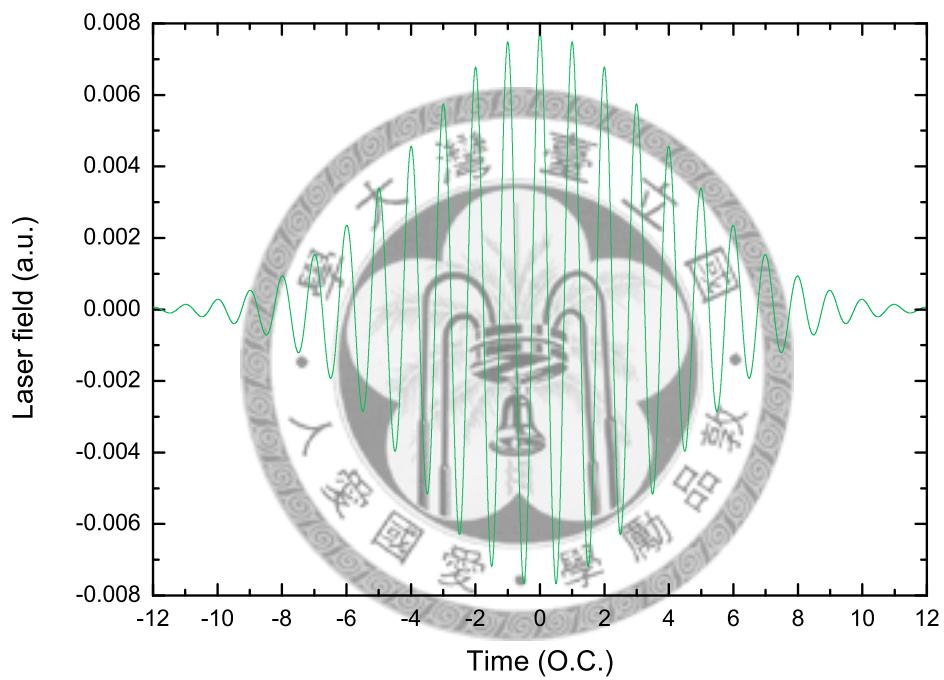


Figure 3.1: Typical laser pulse used in the present calculation. $\lambda = 3600nm$, $\tau_{FWHM} = 110fs$, and $I = 2.1TW/cm^2$.

Once the time-dependent wavefunction is known, we can calculate any physical quantities by computing the expectation values of the corresponding operator. Here we show a few time-dependent quantities closely related to the HHG results in the following sections.

Ion population is defined as

$$\text{Ion population} \equiv 1 - \langle \Psi((r), t) | \Psi((r), t) \rangle. \quad (3.1)$$

The result is shown in Figure 3.2. As we can see, ion population grows rapidly in the

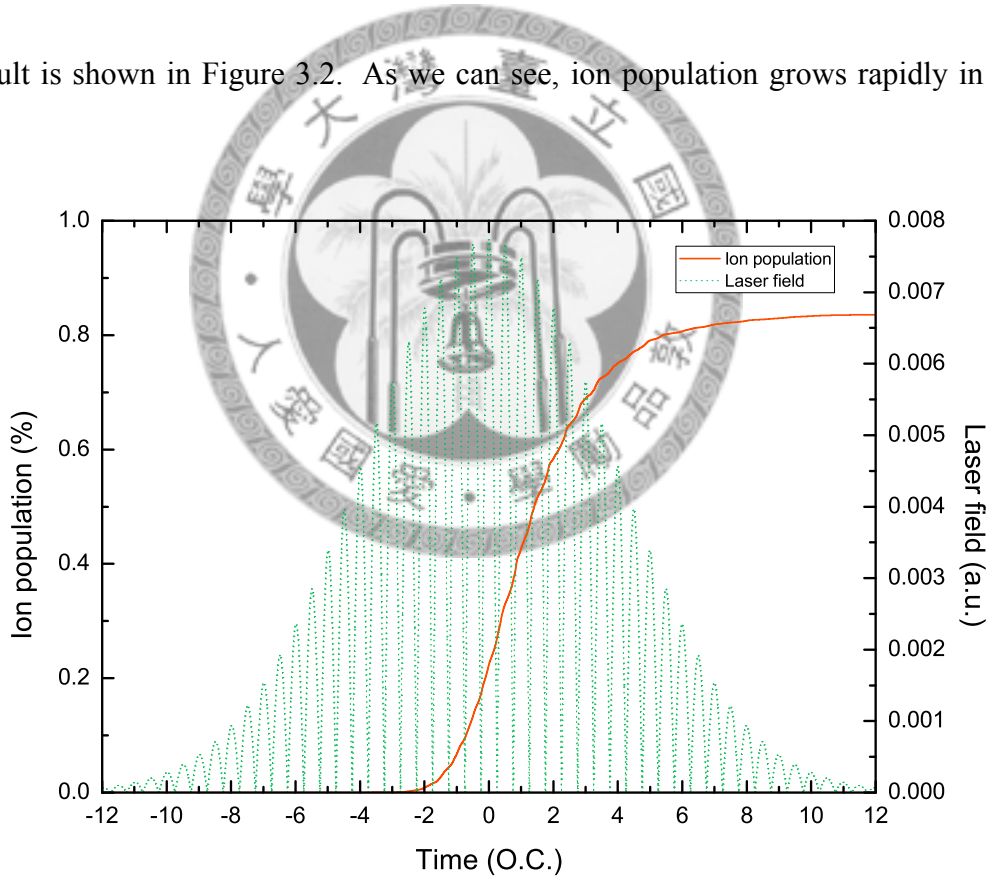


Figure 3.2: Time-dependent ion population (orange solid line). The absolute value of the laser pulse is also shown (green dotted line) for comparison.

middle of the pulse and approaches about 0.86 in the end of the pulse. This ion population is quite high compared with the case of H or other diatomic molecules with similar

Keldysh parameters, and this must have some influence on the HHG, as we will see in the successive sections.

Since radiation originates from the motion of the moving charge, here we also calculate the induced electric dipoles. **Dipole length** has the following expression:

$$d_l(t) \equiv q_e \langle \Psi((r), t) | z | \Psi((r), t) \rangle, \quad (3.2)$$

where the charge of the electron $q_e = -1$. We also calculate the **dipole acceleration** as:

$$d_a(t) \equiv q_e \langle \ddot{z} \rangle. \quad (3.3)$$

The time derivative can be evaluated by the Ehrenfest's theorem:

$$\frac{d}{dt} \langle \Omega \rangle = -i \langle \Phi | [\Omega, H(t)] | \Phi \rangle, \quad (3.4)$$

where Ω is any time-independent operator in Schrödinger's picture, and H is the total Hamiltonian. Incorporating Eqn. 3.4, conservation of angular momentum and parity, and the special structure of the angular-momentum--dependent model potential into Eqn. 3.3,

it becomes:

$$\begin{aligned}
d_a(t) &= \langle \Psi | [[z, H], H] | \Psi \rangle \tag{3.5} \\
&= \langle \Psi | \cos \theta \frac{dV_1}{dr} - F(t) | \Psi \rangle \\
&+ 2\Re \left\{ \langle R_1 | \frac{1}{\sqrt{3}} \frac{d}{dr} \Delta V_0 | R_0 \rangle \right\} \\
&+ 2\Re \left\{ \langle R_1 | \frac{1}{\sqrt{3}} (r \Delta V_0 \frac{P_{l=0}^2}{2} - \frac{P_{l=1}^2}{2} r \Delta V_0) | R_0 \rangle \right\} \\
&- 2\Re \left\{ \langle R_1 | \frac{1}{\sqrt{3}} \frac{\Delta V_0}{r} | R_0 \rangle \right\} \\
&+ 2\Re \left\{ \langle R_1 | \frac{1}{\sqrt{3}} r \Delta V_0^2 | R_0 \rangle \right\} \\
&- 2F(t) \Re \left\{ \langle R_1 | \frac{1}{3} r^2 \Delta V_0 | R_1 \rangle + \langle R_0 | \frac{1}{3} r^2 \Delta V_0 | R_0 \rangle - \langle R_2 | \frac{2}{3\sqrt{5}} r^2 \Delta V_0 | R_0 \rangle \right\},
\end{aligned}$$

where

$$R_l(r, t) \equiv \langle Y_l^0 | \Psi(r, \theta, t) \rangle, \tag{3.6}$$

$$\Delta V_0(r) \equiv V_0(r) - V_1(r), \tag{3.7}$$

and

$$\frac{P_l^2}{2} = -\frac{1}{2} \frac{d^2}{dr^2} + \frac{l(l+1)}{2r^2} \tag{3.8}$$

The results of dipole length and acceleration are shown in Figure 3.3. An interesting phenomenon is that there are some small oscillations in the dipole moments near the end of the pulse. To explore the origin of these oscillations one step further, we compare the dipole accelerations in two different intensities (Figure 3.4). From this figure, we can see that:

- The oscillating frequency is independent of the laser frequency and is estimated to be roughly $4\omega_0$.

- These oscillations become more conspicuous when the laser intensity is relatively low, and persist until the laser field drops nearly to zero.

Since the use of superstrong laser fields tends to wash out the detailed resonant fine structure [41], and the model potential predicts a energy difference about $4.2\omega_0$ between the 6s and 6p states, we may associate these oscillations to the multiphoton resonance between the two strongly coupled bound states.

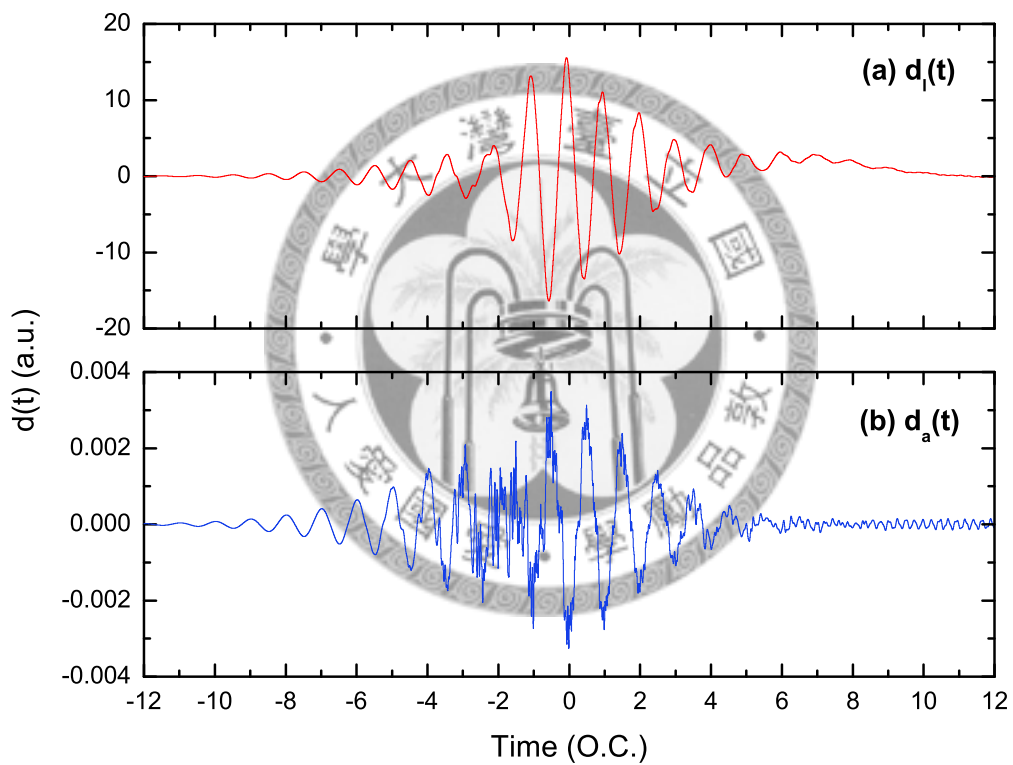


Figure 3.3: Time-dependent induced dipole moment in length form (panel (a)) and acceleration form (panel (b)).

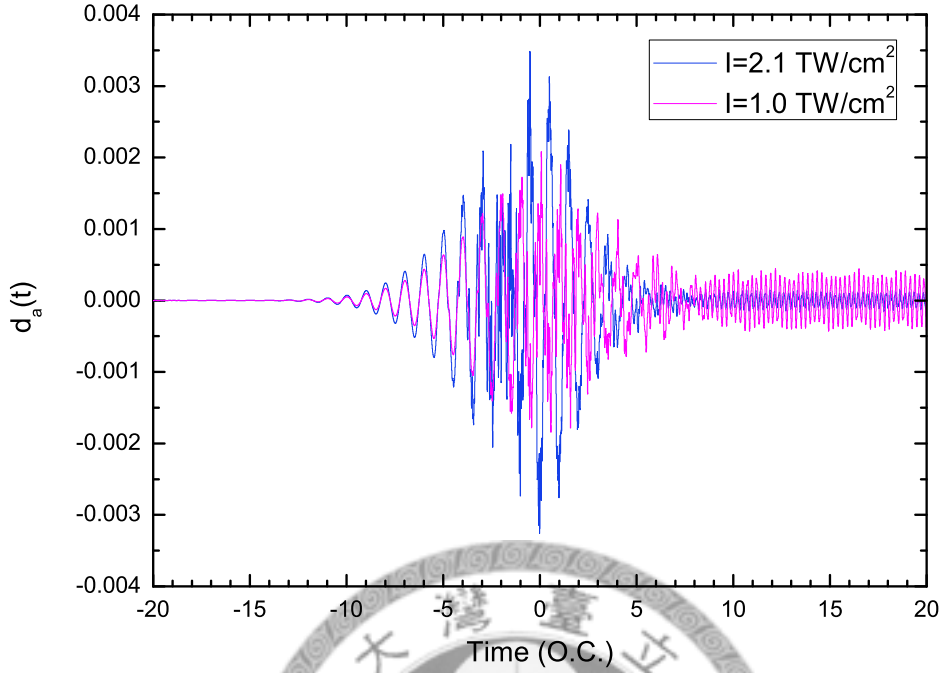


Figure 3.4: Comparison dipole accelerations in two different intensities.

3.2 Fourier analysis: spectral properties of HHG

In this section we show the calculated HHG spectra obtained by Fourier analysis. Here we defined Fourier transformation as:

$$\tilde{d}(\omega) \equiv d(\omega)e^{i\phi(\omega)} = \frac{\int_{t_i}^{t_f} d(t)e^{i\omega t} dt}{t_f - t_i}, \quad (3.9)$$

where $\tilde{d}(\omega)$ is generally complex, and the amplitude $d(\omega)$ and the phase $\phi(\omega)$ are real. As is the definition in [28], the HHG power spectrum can be obtained from

$$D_I(\omega) = d_I^2(\omega), \quad (3.10)$$

or

$$D_a(\omega) = \frac{d_a^2(\omega)}{\omega^4}. \quad (3.11)$$

The agreement of $D_l(\omega)$ and $D_a(\omega)$ is a typical way in our group to make sure the convergency of the calculation. However, the following reasons make the overlapping very hard to achieve for the current case:

- $D_l(\omega)$ weights the contribution of the wavefunction far away from the origin, while $D_a(\omega)$ weights the contribution much closer to the nucleus. For the highly ionized system, converged results based on $D_l(\omega)$ become extremely difficult to obtain, since there is a rising background due to the electron density far from the nucleus and the increasing importance of the interaction of the wavefunction with the edges of the grids, refer to [29] for the detailed numerical experiments and interpretations.
- The equivalence of $D_l(\omega)$ and $D_a(\omega)$ is ensured only if $d_l(t)$ and $\dot{d}_l(t)$ satisfy certain boundary conditions:

$$d_l(t_f) - d_l(t_i) = 0, \quad (3.12)$$

and

$$\dot{d}_l(t_f) - \dot{d}_l(t_i) = 0. \quad (3.13)$$

However, in our numerical experience, the dipole moments for Cs tend to oscillate especially when the pulse is coming to an end or when the laser intensity is low. Thus, the above boundary conditions are generally not established, and $D_l(\omega)$ and $D_a(\omega)$ are not mathematically equivalent.

Therefore, in the current work, we ensure the numerical convergency by doubling one parameter at a time and checking if $D_a(\omega)$ has any change. Hereafter, we will only present

the data based on calculations using $d_a(\omega)$.

In theoretical works, we often calculate the power spectra defined as above. Nonetheless, they actually do not present the *power* emitted by the HHG. According to the classical Larmor formula [42], the instantaneous power emitted is given by

$$P(t) = \frac{2q_e^2}{3c^3} \langle \ddot{z} \rangle^2. \quad (3.14)$$

Hence, we should in fact defined the power spectrum (up to a constant) as

$$P(\omega) = d_a^2(\omega); \quad (3.15)$$

the factor ω^4 is not necessary. In some studies, they present the HHG spectrum as the harmonic yields, i.e. the relative numbers of photons emitted per unit time:

$$\Gamma(\omega) = \frac{d_a^2(\omega)}{\omega}. \quad (3.16)$$

$P(\omega)$ and $\Gamma(\omega)$ are the very physical quantities that experimentalists measure, and they show a more pronounced plateau structure. From now on, we refer to $P(\omega)$ when mentioning HHG power spectra. See Figure 3.5 for the result. The spectrum has several properties:

- There is a clear cut-off at around $35\omega_0$, as same as that predicted by the semi-classical three-step model $E_{cut-off} = I_p + 3.17U_p \cong 34.7\omega_0$.
- There is an additional harmonic peak appearing around $4.17\omega_0$. This corresponds to the strong 6s-6p coupling. The energy difference between the two field-free states

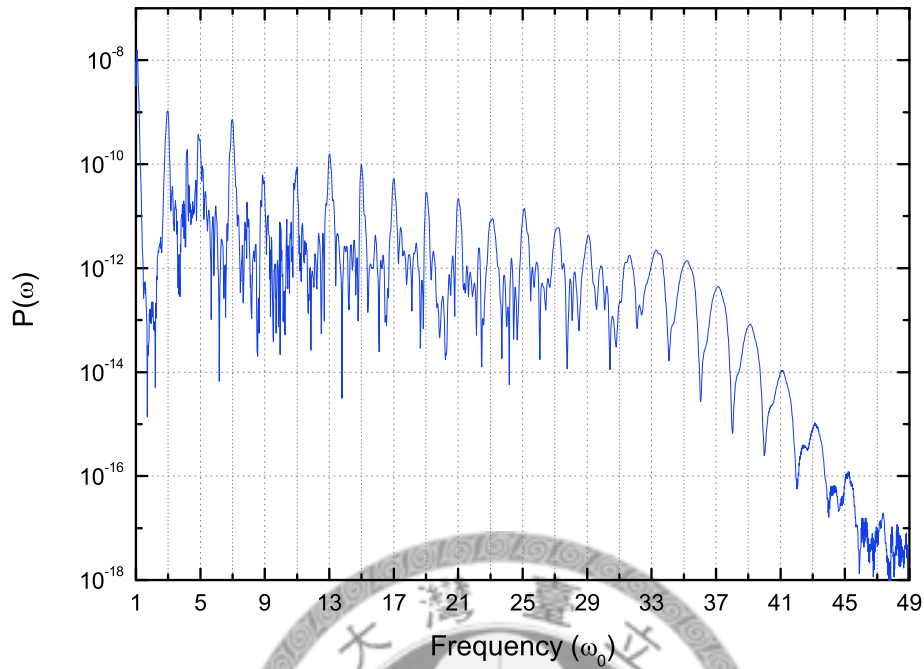


Figure 3.5: Calculated harmonic spectrum $P(\omega)$ from dipole acceleration.

predicted by our model potential is about $4.16\omega_0$.

- The first few harmonics do not show a rapidly declining tendency which is predicted by the perturbation theory. This might have something to do with the resonance effect. The theoretical work studying HHG of Na carried out by Chu et al. [37] shows that the low harmonics could be enhanced by the strong coupling of the ground and the first excited state, and they reveal a much slower decreasing trend compared with that of the non-resonant H atom case.
- There is a plateau in the spectrum: the spectral magnitude from 9th harmonic to 35th cut-off harmonic varies within two orders.
- The shapes of the harmonic peaks near and beyond the cut-off are broad and structureless; the harmonic peaks in the mid-plateau are much narrower; the harmonic

peaks between the two regimes shows peak splitting, for example, the 31st and 33rd harmonics. Similar features can be found in [43, 37].

Let us zoom in to see the below- and near threshold harmonics (harmonic order $q=5-13$) and compare our rescaled result with the experimental data [4]. As we can see, the experimental harmonics show an overall decreasing tendency, while our calculated harmonics do not. The difference of each peak amplitude between the experimental and the theoretical one is not very good, yet within roughly one order of magnitude. The discrepancy is acceptable, since we consider here the single-atom response and not take macroscopic propagation effect into account. We can not compare the peak shapes between these two sets of data, because in [4] they extract the harmonic signals by subtracting the averaged background from the XFROG raw data. Hence the signals are greatly reduced between the successive harmonics.

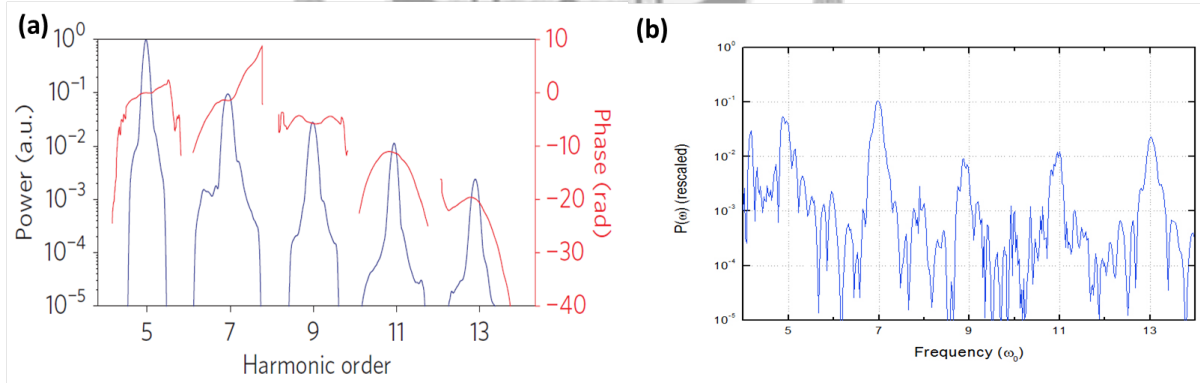


Figure 3.6: Comparison of the below- and near-threshold harmonics. Panel (a) experimental result, reproduced from [4]; panel (b) theoretical result.

Finally we end this section by presenting the HHG power spectrum in a lower laser intensity $I = 1.0TW/cm^2$, see Figure 3.7. Panel (b) shows the whole HHG power spectrum. In this lower intensity, harmonics terminate at a smaller order and there is no clear cut-off due to the fact that Keldysh parameter $\gamma > 1$ here. Note that the 6s-6p resonant

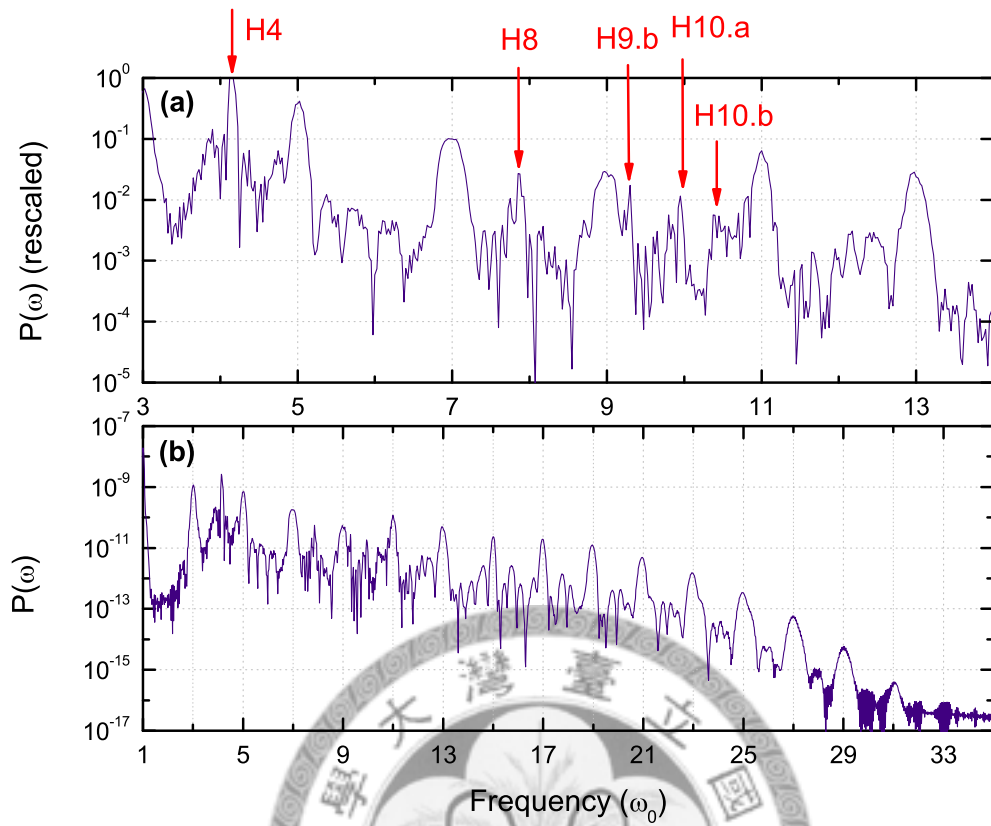


Figure 3.7: HHG power spectrum in the low intensity $I = 1.0 \text{ TW/cm}^2$ case. Panel (a) rescaled below- and near-threshold harmonics; panel (b) the whole HHG spectrum.

structure is more noticeable in this low-intensity case. Now let us look the rescaled low-order harmonics at panel (b). The red arrows label the peaks not belonging to the expected odd harmonics. We might be able to associate these peaks with the 6s-np multiphoton resonances as listed in Table 3.1. Considering the AC Stack shift, the interpretation of the peaks as the resonances between the ground state and some high-lying excited states may sound inappropriate. However, as we can see from the results of the following section, the emission times corresponding to the above harmonics are often near the end of the laser pulse, when the energy shifting is relatively small. Therefore, this correspondence might still be a possible scenario. Work in this direction is in progress in order to provide more sounded understanding of the origin of these peaks.

Table 3.1: Comparison of the positions of the additional harmonic peaks and the field-free 6s- np energy differences calculated by the model potential.

Arrow label	Peak position (ω_0)	Field-free energy difference
H4	4.13	$\Delta E_{6s-6p} = 4.16$
H8	7.87	$\Delta E_{6s-7p} = 7.88$
H9.b	9.23	$\Delta E_{6s-8p} = 9.27$
H10.a	9.94	$\Delta E_{6s-9p} = 9.96$
H10.b	10.39	$\Delta E_{6s-10p} = 10.35$

3.3 Fourier analysis: temporal properties of the HHG

An important aim of this work is to explore the mechanism of the below- and near-threshold harmonics. This involves the cognizance of the *temporal* characteristics of the HHG. The spectral properties of HHG, as we discussed in the last section, only require the knowledge of the spectral amplitudes $d(\omega)$ (see Eqn. 3.9 for the definition), while the spectral phases $\phi(\omega)$ are actually capable of providing us the information about the temporal information of the HHG.

In most of the experimental works, including that done by E. P. Power et al, which characterize the temporal traits of the HHG [4, 44, 45], people measure the *group delay* for each frequency component defined as:

$$\tau_{delay}(\omega) = \frac{\partial \phi}{\partial \omega}. \quad (3.17)$$

This physical quantity has the dimension of time, and it represents the emission time associated a group of harmonics centred on ω . As pointed out in Chapter 1, harmonics due to multiphoton mechanism or tunnelling mechanism can be distinguished by the relative emission times between successive harmonics: for the harmonics generated by multiphoton mechanism, perturbation theory predicts the successive harmonics are emitted

simultaneously (zero chirp), while for the harmonics formed by tunnelling mechanism, the successive harmonics are not emitted in coincidence. In the latter case, we can further discern which kind of trajectories makes the prominent contribution: if the high-frequency harmonic emits *before* the low-frequency one (*negative chirp*), then the *long trajectories* are responsible for this part of HHG; if the high-frequency harmonic emits *after* the low-frequency one (*positive chirp*), then the *short trajectories* are the main generating source. In short, comparing the relative group delays between successive harmonics could give us the answer regarding the mechanism and the channel that lead to the generation of below- and near-threshold harmonics.

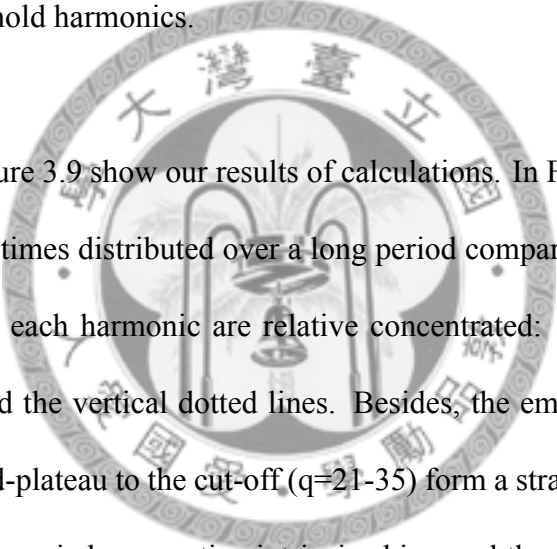


Figure 3.8 and Figure 3.9 show our results of calculations. In Fig 3.8, we can see that although the emission times distributed over a long period compared with the $\tau_{FWHM} = 110fs$, the times near each harmonic are relative concentrated: the distribution of the points is denser around the vertical dotted lines. Besides, the emission times near each harmonic from the mid-plateau to the cut-off ($q=21-35$) form a straight line with negative slope, that is, each harmonic has negative intrinsic chirp, and the magnitude of the chirp rate decreases with q , as predicted by the SFA [46]. Finally, for the frequency where resonance could take place, for example, around $4\omega_0$, $8\omega_0$, $10\omega_0$, the emission times spread over a large range and are relatively late compared with the emission times near other odd harmonics. Figure 3.9 compares the calculated group delays for the below- and near-threshold harmonics with those obtained in the XFROG experiment [4]. Both results reveal the emission times for the harmonic $q=5-13$ show a *non-zero* and *negative slope*, implying tunnelling mechanism, especially the long trajectory, participates the harmonic generation here, in agreement with the conclusion of other recent reports [16, 15, 47].

Note that the our theoretical emission times spread over the range of about 9fs, in good concordance with the experimental results.

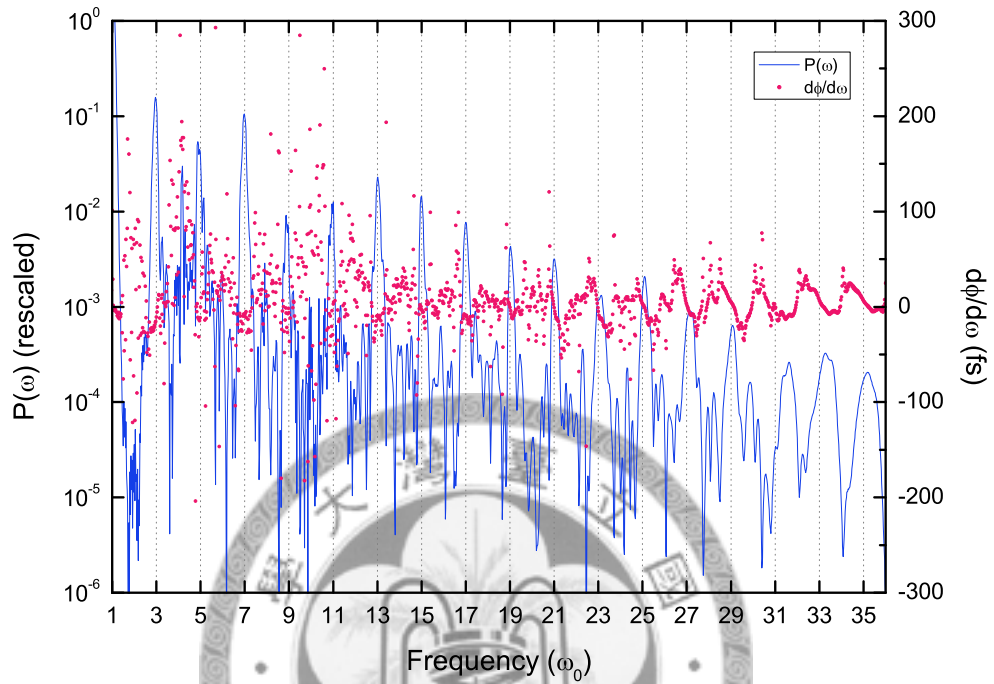


Figure 3.8: Calculate group delay with laser intensity $I = 2.1TW/cm^2$.

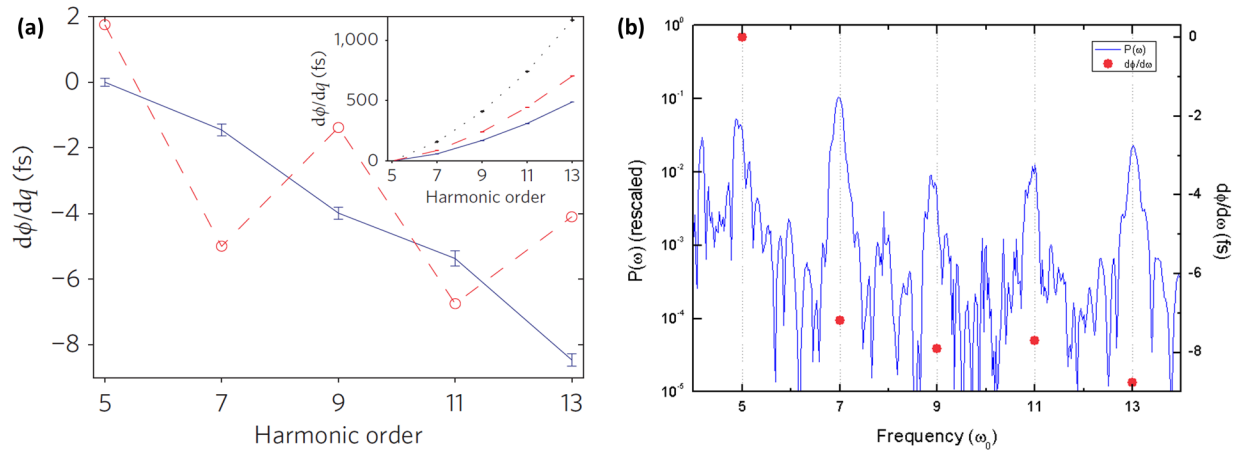


Figure 3.9: Group delay of the below- and near-threshold harmonics. Panel (a) shows the experimental results (blue solid line), reproduced from [4]; panel (b) is our calculated emission times (pink dots).

3.4 Wavelet analysis: spectral and temporal properties of the HHG

In the last section, we dig out some temporal features of the HHG by Fourier transformation and compare them with the experiments. Nevertheless, the emission of the harmonics due to the tunnelling mechanism should appear one per half optical cycle, whenever the laser field reaches a local maxima. Hence, there should be *several* emission times associated with each harmonic. Experimentally, it is impossible to probe the emission times in such a short time scale, so we can only rely on the group delays, which actually represent the *averaged* emission times. Theoretically, however, we are able to extract *every* emission time in a fine temporal resolution: the delicate and non-averaged spectral and temporal characteristics of HHG can be calculated by means of the wavelet transformation.

The wavelet transformation is defined as [48, 43]

$$d_\omega(t) \equiv \int_{t_i}^{t_f} d_a(\bar{t}) \mathcal{W}_{t,\omega}(\bar{t}) d\bar{t}, \quad (3.18)$$

where

$$\mathcal{W}_{t,\omega}(\bar{t}) = \sqrt{\frac{\omega}{\tau}} e^{-\frac{\omega^2(\bar{t}-t)^2}{2\tau^2}} e^{i\omega(\bar{t}-t)}. \quad (3.19)$$

In Fourier transformation, we project the time-dependent physical quantity into plane wave solution, which is *non-localized* in time, thus leads to the lost of the detailed temporal information. Wavelet transformation, on the other side, makes the decomposition using a *localized* wave packet \mathcal{W} with central frequency ω and central emission time t , therefore preserves the minute temporal features. The parameter τ measures the approximate number of oscillations included in the wavelet, and is a compromise between the spectral and temporal resolutions, resulted from the limitation imposed by the uncertainty principle. We have tested the dependence of $d_\omega(t)$ on τ by varying its value from 5 to 30. Although the absolute value of $d_\omega(t)$ changes a little, the general pattern does not change. In the following calculations, we choose $\tau = 13.35$ to perform the wavelet transformation.

Figure 3.10 shows the three-dimensional graph of the modulus of $d_\omega(t)$ in logarithmic scale with respect to various (ω, t) . Figure 3.11 depicts the time profile, i.e. the cross section of the spectrum at a given frequency, for several harmonics in different energy regimes. These figures reveal striking and vivid details of the spectral and temporal structures regarding the HHG mechanisms in different energy regimes:

- For the lowest few harmonic, the 3D spectrum and the time profile (see Figure 3.11 panel (a)) is a smooth function in time. Usually the time profile has a shape mimick-

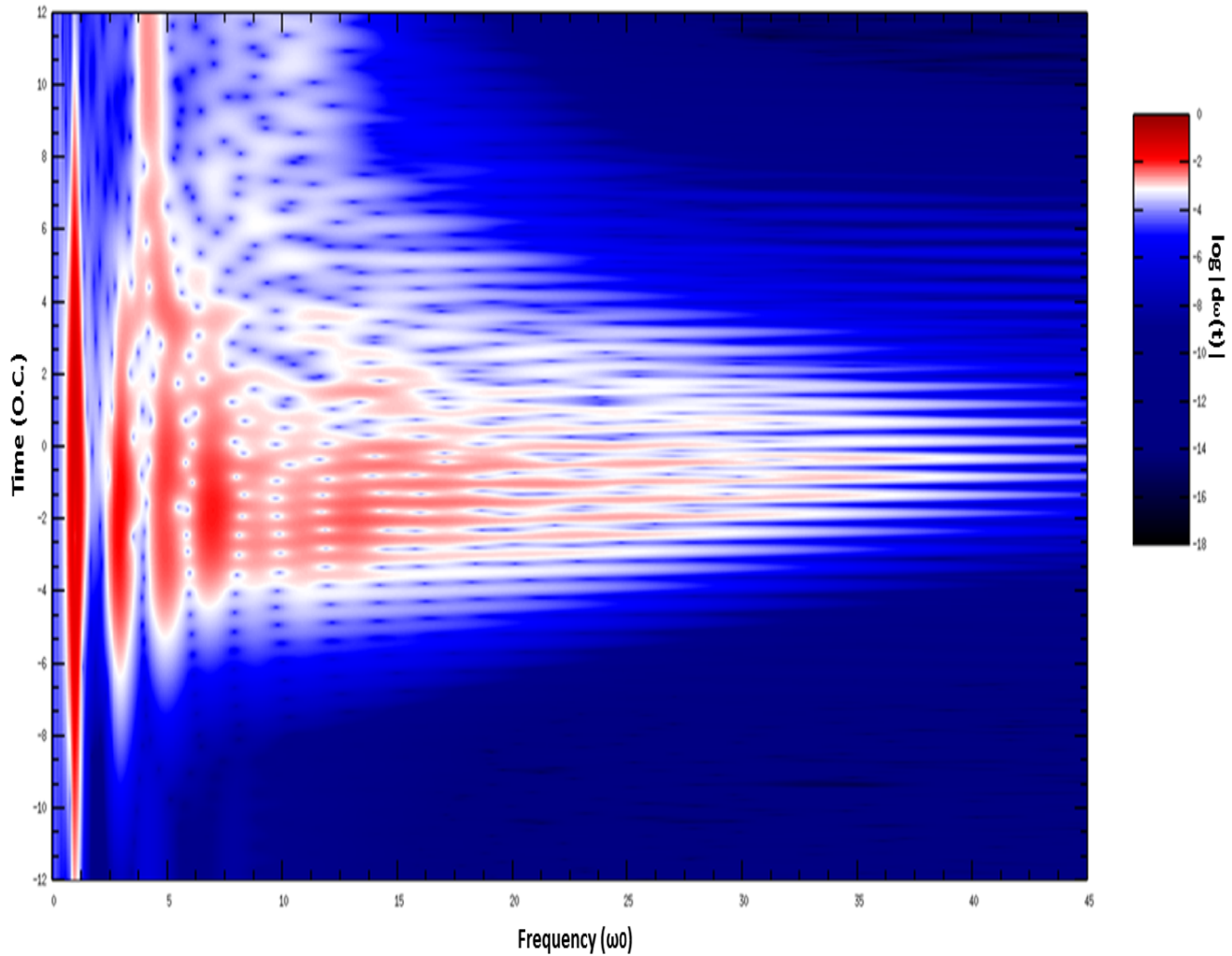


Figure 3.10: Time-frequency spectrum of atomic Cs. The color represent the modulus of $d_{\omega}(t)$ in logarithmic scale.

ing that of the laser envelope (refer to [43] for the H atom case), but our result shows the maxima is shifted toward an earlier time. This may be attributed to the rapid reduction of the bounded electron population (see Figure 3.2), which is not taken into account in the theory. The time profiles in other energy regimes also indicate the similar trends. Anyway, the *smooth* time profile is an evidence that the *multiphoton mechanism* is responsible for the generation of the lowest few harmonics here.

- For the harmonics well above the ionization threshold, the 3D spectrum and the time

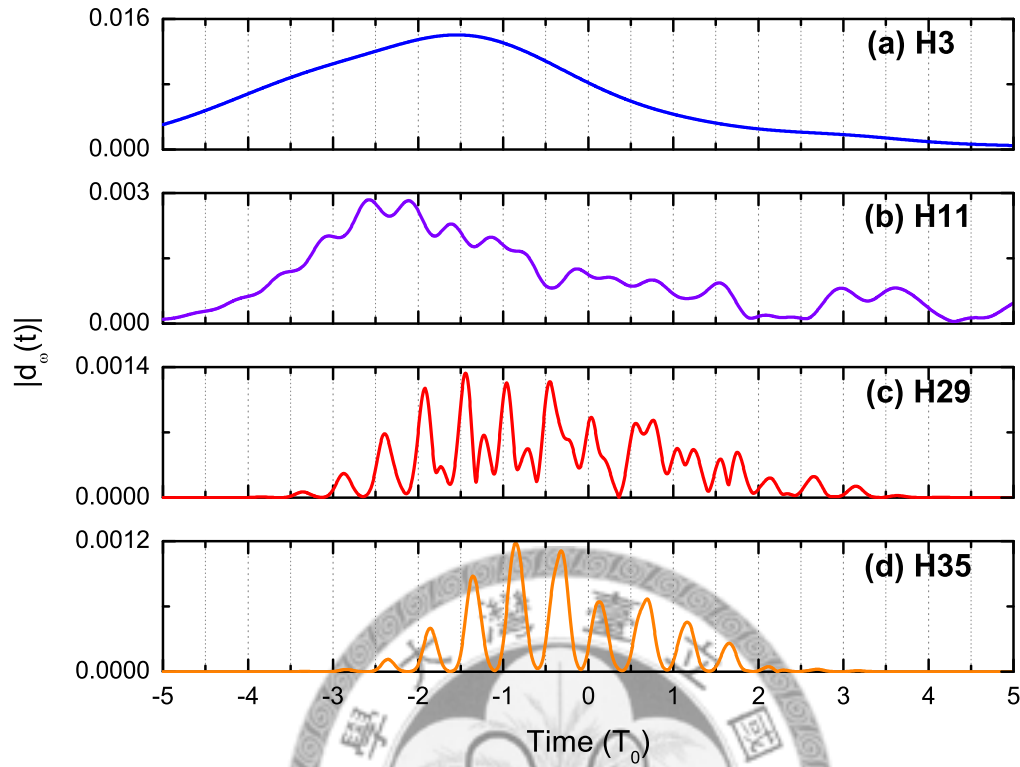


Figure 3.11: Typical time profiles of HHG for (a) the lowest few harmonics, (b) below- and near-threshold harmonics, (c) plateau harmonics, and (d) cut-off harmonics.

profiles (see Figure 3.11 panel (c) and (d)) shows the development of *fast bursts* in time, demonstrating that *tunnelling mechanism* is the prominent mechanism here: the harmonic emission is not only dependent on the envelope of the laser pulse, but is also highly sensitive to the pulse carrier, which decides the crest of the field value and the tunnelling instant. Panel (d) is the time profile for the 35th harmonic in the cut-off, from which we can see that there is one burst per half optical cycle, while Panel (c) is the time profile for the harmonic in the plateau, from which we can tell that there are two bursts per half O.C. in the middle of the pulse. These findings are in accordance with what predicted by the semi-classical three-step model: there are two channels, namely the long and short trajectories, contributing to the generation

of plateau harmonics, and these channels merge together for the harmonics in the cut-off.

- From the above two points, we know that the 3D spectrum of the lowest few harmonics are characterized by the vertical bands, while the spectrum of high harmonics are characterized by horizontal lines. For the harmonics between the two extremes, the spectrum show a *net-like* structures due to the competition of the multiphoton and tunnelling mechanisms. The **below- and near-threshold (5th to 13th) harmonics obviously lie in this net-like regime**. Figure 3.12 plots the evolution of the time profile for the below- and near-thresholds harmonics. The existence of fast bursts is discernible for the harmonic orders greater than 7.

- For the harmonic at a frequency slight greater than $4\omega_0$, the 3D spectrum shows an almost continuous emission especially when the laser pulse is coming to an end. The time profile at $\omega = 4.2\omega_0$ is presented in Figure 3.13. We may attributed this to the multiphoton resonance between the strongly coupled $6s$ and $6p$ states. The information we get by the wavelet transformation is consistent with these we obtain from the time-dependent dipole moments (Figure 3.3 and 3.4) and the time delays (Figure 3.8). There are other extended structures below the ionization threshold near the end of the pulse, but we can not specify them with some clear frequency components. The physical origin in this regime needs further investigation.

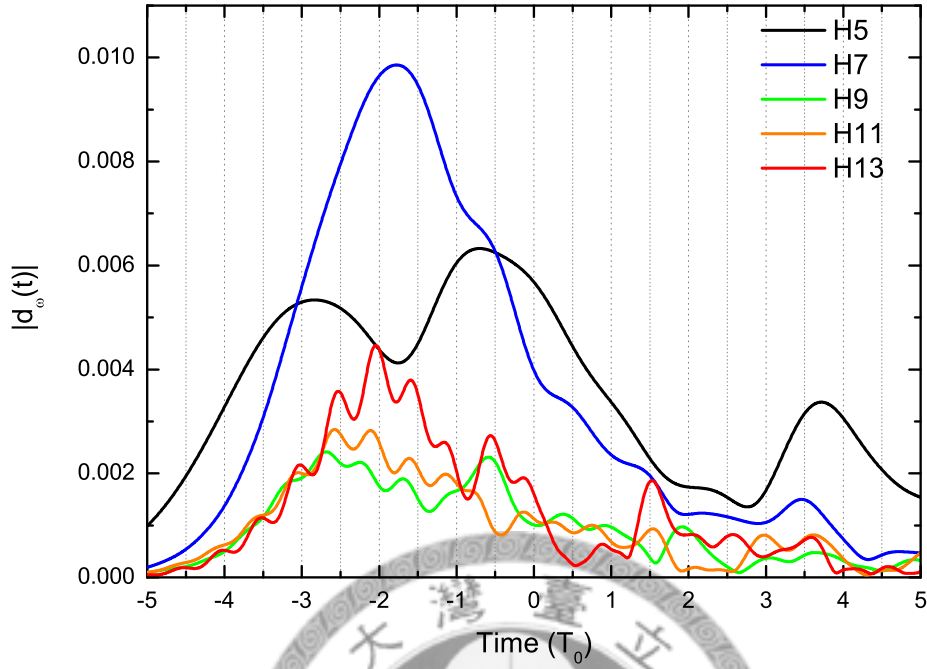


Figure 3.12: Evolution of the time profiles of the below- and near-threshold harmonics.

3.5 Summary

In this chapter, first we discuss the quantum dynamics, then we explore the spectral and temporal characteristics of the HHG of atomic Cs in mid-infrared laser pulses by Fourier transformation and the wavelet analysis. The strong couplings between $6s$ and np states, $6s$ and $6p$ in particular, producing notable peaks in addition to the expected odd harmonics when the laser field is relatively weak. Both the results of Fourier and wavelet transformations verify the existence of the tunnelling mechanism (besides the multiphoton mechanism) for the below- and near-threshold harmonics. We further indicate that the contribution from the tunnelling mechanism is through the channel of long trajectories by showing the negative chirp in the calculated group delays, which is in good agreement compared with the experimental result [4].

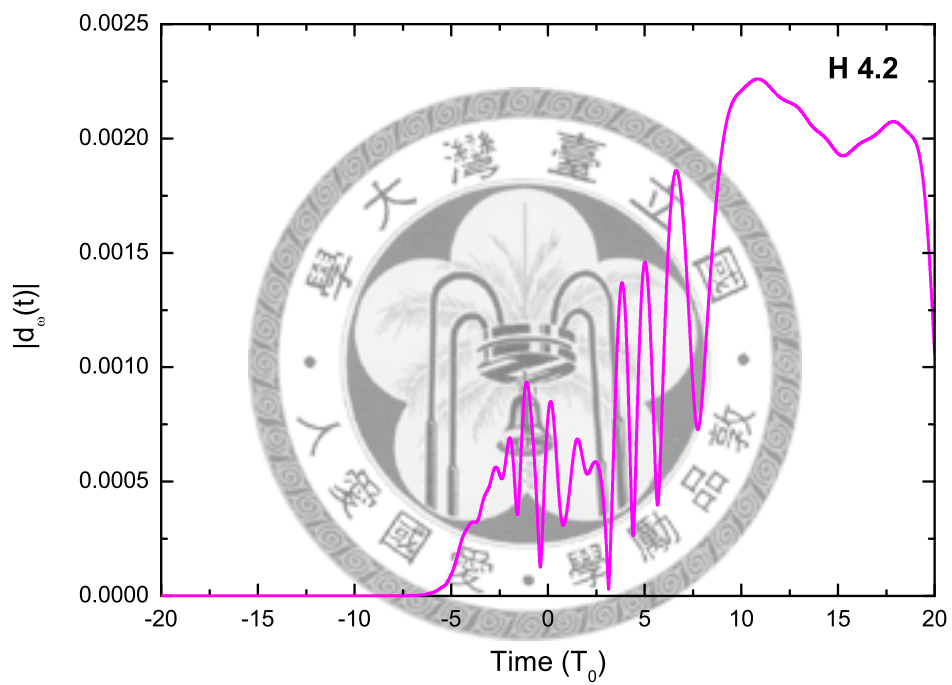
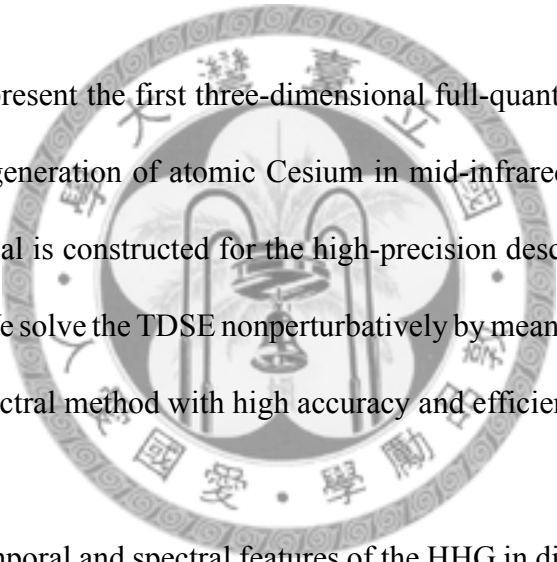


Figure 3.13: Typical time profile for a peak due to the multiphoton resonance between two strongly coupled states, here the $6s$ and $6p$ states.

Chapter 4

Conclusions and Future Perspectives



In this thesis, we present the first three-dimensional full-quantum calculations of the high-order harmonic generation of atomic Cesium in mid-infrared laser pulses. A one-electron model potential is constructed for the high-precision description of the Cs atom electronic structure. We solve the TDSE nonperturbatively by means of the time-dependent generalized pseudospectral method with high accuracy and efficiency.

We analyze the temporal and spectral features of the HHG in different energy regimes by performing Fourier and wavelet transformations. One special property of the HHG of atomic Cs is the extra peaks in addition to the normal odd harmonics. These peaks result from the strong couplings between the $6s$ and np states and become more salient when the laser field is relatively weak, for example, when the laser pulse is coming to an end or a lower peak intensity is used. We also address the problem of the mechanisms of the below- and near-threshold harmonics. The calculated group delays show these harmonics are negatively chirped and imply long trajectories due to tunnelling mechanism work here; both the trend and magnitude of the theoretical results are in good agreement the experi-

mental values [4]. Wavelet transformation reveals the detailed time-frequency spectrum of below- and near-threshold harmonics have a net-like structure, demonstrating in another way that both the multiphoton and tunnelling mechanisms participate the harmonic generation in this energy regime. By comparing the calculated emission times from the wavelet transformation with those predicted by classical simulations, we hope in the near future we can unwrap and identify the contributions from different types of trajectories and explain how they function for the generation of below- and near-threshold harmonics.

We show the importance of the strongly coupled $6s - np$ states in this work by the existence of additional peaks in the spectra. However, the competition and interference between the $continuum \rightarrow 6s$ and the $continuum \rightarrow 6p$ should affect the whole HHG spectra in some way. This effect has already be found experimentally to cause the appearance of some side peaks in the above-threshold ionization (ATI) photoelectron spectra [17], yet no studies on the HHG photon spectra have been performed. The theoretical understanding of the resonant effect may also bring some practical applications. For example, it may be possible to use a second *coupling* laser beam as a means for the active control of the HHG process by tuning the populations in the two states [18]. We shall continue our work in this direction.

Bibliography

- [1] M. Ferray and et al. Multiple-harmonic conversion of 1064 nm radiation in rare gases. *Journal of Physics B: Atomic, Molecular and Optical Physics*, 21(3):L31, 1988.
- [2] P. B. Corkum and F. Krausz. Attosecond science. *Nature Physics*, 3(6):381--387, 2007.
- [3] A. M. March. Strong field studies of cesium using intense mid-infrared light. *PhD thesis, Stony Brook University*, 2009.
- [4] E. P. Power, A. M. March, F. Catoire, E. Sistrunk, K. Krushelnick, P. Agostini, and L. F. DiMauro. Xfrog phase measurement of threshold harmonics in a keldysh-scaled system. *Nature Photonics*, 4(6):352--356, 2010.
- [5] J. E. Sansonetti. Wavelengths, transition probabilities, and energy levels for the spectra of cesium (cs i--cs iv). *Journal of Physical and Chemical Reference Data*, 38(4):761--923, 2009.
- [6] P. Colosimo, G. Doumy, C. I. Bologa, J. Wheeler, C. Hauri, F. Catoire, J. Tate, R. Chirla, A. M. March, G. G. Paulus, H. G. Muller, P. Agostini, and L. F. DiMauro. Scaling strong-field interactions towards the classical limit. *Nature Physics*, 4(5): 386--389, 2008.

- [7] Zenghu Chang, Andy Rundquist, Haiwen Wang, Margaret M. Murnane, and Henry C. Kapteyn. Generation of coherent soft x rays at 2.7 nm using high harmonics. *Physical Review Letters*, 79(16):2967, 1997.
- [8] Ch. Spielmann, N. H. Burnett, S. Sartania, R. Koppitsch, M. Schnürer, C. Kan, M. Lenzner, P. Wobrauschek, and F. Krausz. Generation of coherent x-rays in the water window using 5-femtosecond laser pulses. *Science*, 278(5338):661--664, 1997.
- [9] E. Goulielmakis, M. Schultze, M. Hofstetter, V. S. Yakovlev, J. Gagnon, M. Uiberacker, A. L. Aquila, E. M. Gullikson, D. T. Attwood, R. Kienberger, F. Krausz, and U. Kleineberg. Single-cycle nonlinear optics. *Science*, 320(5883):1614--1617, 2008.
- [10] E. Gustafsson, T. Ruchon, M. Swoboda, T. Remetter, E. Pourtal, R. Lopez-Martens, P. Balcou, and A. L'Huillier. Broadband attosecond pulse shaping. *Optics Letters*, 32(11):1353--1355, 2007.
- [11] L. V. Keldysh. Ionization in field of a strong electromagnetic wave. *Soviet Physics JETP-USSR*, 20(5):1307--1308, 1965.
- [12] P. B. Corkum. Plasma perspective on strong field multiphoton ionization. *Physical Review Letters*, 71(13):1994, 1993.
- [13] Jeffrey L. Krause, Kenneth J. Schafer, and Kenneth C. Kulander. High-order harmonic generation from atoms and ions in the high intensity regime. *Physical Review Letters*, 68(24):3535, 1992.

- [14] A. Lhuillier, K. J. Schafer, and K. C. Kulander. Theoretical aspects of intense field harmonic-generation. *Journal of Physics B-Atomic Molecular and Optical Physics*, 24(15):3315--3341, 1991.
- [15] H. Soifer, P. Botheron, D. Shafir, A. Diner, O. Raz, B. D. Bruner, Y. Mairesse, B. Pons, and N. Dudovich. Near-threshold high-order harmonic spectroscopy with aligned molecules. *Physical Review Letters*, 105(14):143904, 2010.
- [16] D. C. Yost, T. R. Schibli, J. Ye, J. L. Tate, J. Hostetter, M. B. Gaarde, and K. J. Schafer. Vacuum-ultraviolet frequency combs from below-threshold harmonics. *Nature Physics*, 5(11):815--820, 2009.
- [17] W. Nicklich, Kumpfm, uuml, H. Iler, H. Walther, X. Tang, Huale Xu, and P. Lambropoulos. Above-threshold ionization of cesium under femtosecond laser pulses: New substructure due to strongly coupled bound states. *Physical Review Letters*, 69(24):3455, 1992.
- [18] B. Sheehy, J. D. D. Martin, L. F. DiMauro, P. Agostini, K. J. Schafer, M. B. Gaarde, and K. C. Kulander. High harmonic generation at long wavelengths. *Physical Review Letters*, 83(25):5270, 1999.
- [19] B. Sheehy, T. O. Clatterbuck, C. Lyng, J. D. D. Martin, D. W. Kim, L. F. DiMauro, M. B. Gaarde, K. J. Schafer, P. Agostini, and K. C. Kulander. Strong field physics in a scaled interaction. *Laser Physics*, 11(2):226--230, 2001.
- [20] Mette B. Gaarde and Kenneth J. Schafer. Enhancement of many high-order harmonics via a single multiphoton resonance. *Physical Review A*, 64(1):013820, 2001.

- [21] G. Doumy, J. Wheeler, E. Sistrunk, A. DiChiara, T. A. Miller, E. Power, A. M. March, F. Catoire, C. Blaga, I. Lachko, C. Roedig, R. Chirila, K. Krushelnick, P. Agostini, and L. F. DiMauro. High harmonic generation from long wavelength drivers. In *Lasers Electro Optics The Pacific Rim Conference on Lasers and Electro-Optics, 2009. CLEO/PACIFIC RIM '09. Conference on*, pages 1--2.
- [22] T. O. Clatterbuck, C. Lynga, P. Colosimo, J. D. D. Martin, B. Sheehy, L. F. DiMauro, P. Agostini, and K. C. Kulander. Scaled intense laser-atom physics: the long wavelength regime. *Journal of Modern Optics*, 50:441--450, 2003.
- [23] T. O. Clatterbuck, Lyng, aring, C., P. M. Paul, L. F. DiMauro, M. B. Gaarde, K. J. Schafer, P. Agostini, K. C. Kulander, and I. Walmsley. Yield and temporal characterization of high-order harmonics from intense midinfrared excitation of a cesium vapor. *Physical Review A*, 69(3):033807, 2004.
- [24] M. Lewenstein, Ph Balcou, M. Yu Ivanov, Anne L'Huillier, and P. B. Corkum. Theory of high-harmonic generation by low-frequency laser fields. *Physical Review A*, 49(3):2117, 1994.
- [25] P. Salières, B. Carré, L. Le Déroff, F. Grasbon, G. G. Paulus, H. Walther, R. Kopold, W. Becker, D. B. Milošević, A. Sanpera, and M. Lewenstein. Feynman's path-integral approach for intense-laser-atom interactions. *Science*, 292(5518):902--905, 2001.
- [26] Zhangjin Chen, Toru Morishita, Anh-Thu Le, and C. D. Lin. Analysis of two-dimensional high-energy photoelectron momentum distributions in the single ionization of atoms by intense laser pulses. *Physical Review A*, 76(4):043402, 2007.

- [27] Shih-I. Chu and Dmitry A. Telnov. Beyond the floquet theorem: generalized floquet formalisms and quasienergy methods for atomic and molecular multiphoton processes in intense laser fields. *Physics Reports*, 390(1-2):1--131, 2004.
- [28] X. M. Tong and S. I. Chu. Theoretical study of multiple high-order harmonic generation by intense ultrashort pulsed laser fields: A new generalized pseudospectral time-dependent method. *Chemical Physics*, 217(2-3):119--130, 1997.
- [29] Jeffrey L. Krause, Kenneth J. Schafer, and Kenneth C. Kulander. Calculation of photoemission from atoms subject to intense laser fields. *Physical Review A*, 45(7):4998, 1992.
- [30] G. H. Yao and S. I. Chu. Generalized pseudospectral methods with mappings for bound and resonance state problems. *Chemical Physics Letters*, 204(3-4):381--388, 1993.
- [31] D. A. Telnov and S. I. Chu. Multiphoton detachment of h^- near the one-photon threshold: Exterior complex-scaling-generalized pseudospectral method for complex quasienergy resonances. *Physical Review A*, 59(4):2864--2874, 1999.
- [32] J. Y. Wang, S. I. Chu, and C. Laughlin. Multiphoton detachment of h^- . 2. intensity-dependent photodetachment rates and threshold behavior - complex-scaling generalized pseudospectral method. *Physical Review A*, 50(4):3208--3215, 1994.
- [33] M. R. Hermann and J. A. Fleck. Split-operator spectral method for solving the time-dependent schrodinger-equation in spherical coordinates. *Physical Review A*, 38(12):6000--6012, 1988.

- [34] Xiao-Min Tong and Shih-I. Chu. Time-dependent approach to high-resolution spectroscopy and quantum dynamics of rydberg atoms in crossed magnetic and electric fields. *Physical Review A*, 61(3):031401, 2000.
- [35] Juan J. Carrera, X. M. Tong, and Shih-I. Chu. Creation and control of a single coherent attosecond xuv pulse by few-cycle intense laser pulses. *Physical Review A*, 74(2):023404, 2006.
- [36] Juan J. Carrera and Shih-I. Chu. Extension of high-order harmonic generation cutoff via coherent control of intense few-cycle chirped laser pulses. *Physical Review A*, 75(3):033807, 2007.
- [37] X. Chu, S. I. Chu, and C. Laughlin. Spectral and temporal structures of high-order harmonic generation of na in intense mid-ir laser fields. *Physical Review A*, 6401(1):-, 2001.
- [38] D. A. Telnov and S. I. Chu. Ab initio study of the orientation effects in multiphoton ionization and high-order harmonic generation from the ground and excited electronic states of h(2)(+). *Physical Review A*, 76(4), 2007.
- [39] X. Chu and S. I. Chu. Self-interaction-free time-dependent density-functional theory for molecular processes in strong fields: High-order harmonic generation of h-2 in intense laser fields. *Physical Review A*, 6302(2):--, 2001.
- [40] J. Heslar, D. Telnov, and S. I. Chu. High-order-harmonic generation in homonuclear and heteronuclear diatomic molecules: Exploration of multiple orbital contributions. *Physical Review A*, 83(4), 2011.

- [41] Shih-I. Chu. Quasienergy formalism for intense field multiphoton ionization of atoms induced by circularly polarized radiation. *Chemical Physics Letters*, 54(2): 367--372, 1978.
- [42] B. Sundaram and P. W. Milonni. High-order harmonic-generation - simplified model and relevance of single-atom theories to experiment. *Physical Review A*, 41(11): 6571--6573, 1990.
- [43] X. M. Tong and S. I. Chu. Probing the spectral and temporal structures of high-order harmonic generation in intense laser pulses. *Physical Review A*, 6102(2):--, 2000.
- [44] Y. Mairesse, A. de Bohan, L. J. Frasinski, H. Merdji, L. C. Dinu, P. Monchicourt, P. Breger, M. Kovacev, R. Taieb, B. Carre, H. G. Muller, P. Agostini, and P. Salieres. Attosecond synchronization of high-harmonic soft x-rays. *Science*, 302(5650):1540-1543, 2003.
- [45] G. Doumy, J. Wheeler, C. Roedig, R. Chirla, P. Agostini, and L. F. DiMauro. Attosecond synchronization of high-order harmonics from midinfrared drivers. *Physical Review Letters*, 102(9):093002, 2009.
- [46] Mette Gaarde. Time-frequency representations of high order harmonics. *Opt. Express*, 8(10):529--536, 2001.
- [47] James A. Hostetter, Jennifer L. Tate, Kenneth J. Schafer, and Mette B. Gaarde. Semiclassical approaches to below-threshold harmonics. *Physical Review A*, 82(2): 023401, 2010.

- [48] Philippe Antoine, Bernard Piraux, and Alfred Maquet. Time profile of harmonics generated by a single atom in a strong electromagnetic field. *Physical Review A*, 51(3):R1750, 1995.

